

An Interpretation of Flare-Induced and Decayless Coronal-Loop Oscillations as Interference Patterns

Bradley W. Hindman

*JILA and Department of Astrophysical and Planetary Sciences, University of Colorado,
Boulder, CO 80309-0440, USA*

Rekha Jain

School of Mathematics & Statistics, University of Sheffield, Sheffield S3 7RH, UK

hindman@solarz.colorado.edu

ABSTRACT

We present an alternative model of coronal-loop oscillations which considers that the waves are trapped in a 2D waveguide formed by the entire arcade of field lines. This differs from the standard 1D model which treats the waves as the resonant oscillations of just the visible bundle of field lines. Within the framework of our 2D model, the two types of oscillations that have been observationally identified, flare-induced waves and “decayless” oscillations, can both be attributed to MHD fast waves. The two components of the signal differ only because of the duration and spatial extent of the source that creates them. The flare-induced waves are generated by strong localized sources of short duration, while the decayless background can be excited by a continuous, stochastic source. Further, the oscillatory signal arising from a localized, short-duration source can be interpreted as a pattern of interference fringes produced by waves that have traveled diverse routes of various pathlengths through the waveguide. The resulting amplitude of the fringes slowly decays in time with an inverse square root dependence. The details of the interference pattern depend on the shape of the arcade and the spatial variation of the Alfvén speed. The rapid decay of this wave component, which has previously been attributed to physical damping mechanisms that remove energy from resonant oscillations, occurs as a natural consequence of the interference process without the need for local dissipation.

Subject headings: MHD — waves — Sun: Corona — Sun: magnetic fields

1. Introduction

The detection of standing kink-wave oscillations on bright coronal loops by the TRACE instrument (e.g., Aschwanden et al. 1999; Nakariakov et al. 1999) proffered the possibility that seismic techniques could be applied to magnetic structures in the corona. Given that the magnetic field of the corona remains resistant to measurement by spectroscopic means, coronal-loop seismology permits the direct probing of an otherwise inaccessible (yet paramount) property of the corona. Two observational details suggest that many of the observed motions are those arising from resonant standing waves with wavelengths corresponding to the fundamental mode. These observational details are that different segments of the loop are often observed to vascillate in phase with each other and the sinuous motion usually lacks nodes, except perhaps at the loop footpoints. In some instances in addition to the fundamental mode with the lowest frequency, coexistent overtones (with interior nodes and a higher frequency) have been detected (Verwichte et al. 2004; Van Doorselaere et al. 2007; De Moortel & Brady 2007). The discovery of such overtones precipitated a tumult of theoretical activity with the goals of both explaining the observed dispersion and developing seismic methods that use the dispersion to surmise the field strength and mass density along the loop (see the review by Andries et al 2009).

The first oscillations to be detected were the response of loops within coronal arcades to the passage of transient disturbances launched from solar flares. It has been observed that such oscillations, once initiated, rapidly diminish over 3–4 wave periods (e.g., White & Verwichte 2012). A variety of theoretical studies have suggested possible damping mechanisms to explain the observed diminuation of the signal, with the most prominent being resonant absorption (e.g., Ruderman & Roberts 2002; Goossens et al. 2002, 2011) and phase mixing between distinct fibrils in a bundle, each with slightly different wave speeds (Ofman & Aschwanden 2002). In all cases the diminuation of signal results from a physical loss of energy from the observed kink waves.

Recent observations (Nisticò et al. 2013; Anfinogentov et al. 2013) using the Atmospheric Imaging Assembly (AIA) on the Solar Dynamics Observatory (SDO) have revealed that in addition to these large-amplitude flare-induced oscillations there appears to be a continuous background of fluctuating power that oscillates at frequencies similar to the flare-induced waves, but with a lower amplitude that does not exhibit significant attenuation. These studies have posited that the background oscillations are excited by a continuous, and perhaps stochastic, driver whose energy input is balanced on the long term by physical damping. Thus, the two classes of oscillation are caused by waves with the same resonant nature, but excited by different sources, one ongoing and the other impulsive.

Implicit in much of this prior work is the assumption that each visible loop in a coronal

arcade is essentially an independent wave cavity. The MHD kink waves are presumed to have a group velocity that is parallel to the field lines and each loop oscillates as a coherent entity. Thus, the problem is reduced to a 1D wave problem and any decay in the signal must be due to a physical loss of energy. Here we explore an alternative interpretation. Two properties of the observed oscillations suggest that the wave cavity may be inherently 2D instead of 1D. The first of these properties is that most oscillating loops appear to be part of a coronal arcade and that flares often cause the entire arcade to ring and throb. The second property is that most of the standing waves that have been observed possess a “horizontal” polarization such that the loop sways back and forth within the arcade without significant expansion and contraction of the loop’s radius. This implies that the motion of a loop impacts neighboring (and possibly invisible) field lines within the arcade and forces them to move. The individual bundles of field lines that form loops are therefore not isolated from the larger arcade structure in which they are embedded. Previously, the ringing of the arcade has been interpreted to be the transient disturbance, launched by the flare, that excites the resonant oscillations separately on each field line. Here we suggest that the arcade forms a 2D waveguide and that the ringing is a superposition of waveguide modes that form in response to driving by flares and other sources. The waves are inherently 2D modes that are trapped standing waves longitudinal to the field, while propagating up and down the axis of the arcade perpendicular to the field. We will find that such a model naturally leads to decaying signals without the need for a physical damping mechanism. The attenuation of the sinusoidal signal observed at a given field line or loop is a fringe pattern resulting from the self interference of a wavefront as it expands away from a point source.

In Section 2 we derive a simple wave equation that describes MHD fast waves that propagate on a thin 2D sheet of arching field lines. We define the geometry of the field and describe the boundary conditions that turn the arcade into a waveguide. In Section 3 we derive the response of the waveguide to two types of sources, a continuous stochastic source and an impulsive source. Finally, in Section 4 we discuss the implications of our calculation and present our conclusions.

2. MHD Fast Waves in a Waveguide

We treat a coronal arcade as a thin magnetized sheet with each field line in the sheet piercing the photosphere at two locations. The locus of the footpoints for all of the field lines form two parallel lines in the photosphere. If we view the photosphere as a dense, immovable fluid, waves are trapped between the footpoints and the arcade acts as a 2D waveguide for MHD fast waves that permits free propagation up and down its axis perpendicular to the

field. We utilize a Cartesian coordinate system oriented such that the x – y plane corresponds to the photosphere and the z coordinate is the height above the photosphere. Let the arcade be invariant in the y -direction and let it lack shear such that the field has no component in that direction,

$$\mathbf{B} = B_x(x, z)\hat{\mathbf{x}} + B_z(x, z)\hat{\mathbf{z}} . \quad (2.1)$$

Figure 1 provides a schematic diagram of the arcade and its geometry.

For simplicity, we will assume that the corona is magnetically dominated such that gravity and gas pressure can be ignored when compared to the magnetic forces. Furthermore, in order to build an illustrative example without unnecessary mathematical complication, we will ignore the curvature of the field lines within the wave equation and assume that the Alfvén speed V_A within the sheet is uniform. With these assumptions, fast MHD waves can be conveniently expressed using local Frenet coordinates. The triad of unit vectors that represents this local coordinate system are the tangent to the field line $\hat{\mathbf{s}}$, the field line’s principal normal $\hat{\boldsymbol{\eta}}$, and the binormal $\hat{\boldsymbol{\gamma}}$. The tangential coordinate s measures the pathlength along a field line starting from the photosphere, with the footpoints located at $s = 0$ and $s = L$, where the length of each field line L is the same. The coordinate y marks distance along the axis of the waveguide and we assume that the arcade is long enough that we can ignore edge effects.

2.1. Equation for Driven Fast Waves

Since we are only considering magnetic forces, fast MHD waves lack motion parallel to the field lines and the transverse motion is irrotational,

$$\mathbf{v} = v\hat{\boldsymbol{\gamma}} + w\hat{\boldsymbol{\eta}} , \quad (2.2)$$

$$\frac{\partial v}{\partial \eta} = \frac{\partial w}{\partial y} . \quad (2.3)$$

Further, driven fast waves satisfy the following simple equation,

$$\left[\frac{\partial^2}{\partial t^2} - V_A^2 \left(\frac{\partial^2}{\partial y^2} + \frac{\partial^2}{\partial s^2} + \frac{\partial^2}{\partial \eta^2} \right) \right] \mathbf{v} = \mathbf{S}(\mathbf{x}, t) , \quad (2.4)$$

where $\mathbf{S}(\mathbf{x}, t)$ is a wave driver, the Alfvén speed V_A is given by $V_A^2 = B^2/4\pi\rho$, and ρ is the mass density. In observational contexts, motions in the direction of the principal normal, w , are often referred to as “vertical” oscillations, whereas velocities v in the binormal direction, along the axis of the arcade, are called “horizontal” oscillations. We will explore horizontal oscillations ($w = 0$) by supposing that the driver only acts in the binormal direction and lacks variation across the arcade’s sheet, i.e., the driver is independent of the coordinate η . With these assumptions, only 2D wave modes are excited and they obey the following equation:

$$\left[\frac{\partial^2}{\partial t^2} - V_A^2 \left(\frac{\partial^2}{\partial y^2} + \frac{\partial^2}{\partial s^2} \right) \right] v = S(s, y, t) . \quad (2.5)$$

We make the arcade into a waveguide by imposing boundary conditions at the footpoints. Specifically, we apply the line tying condition at the photosphere (i.e., $v = 0$ at $s = 0$ and $s = L$). The resonant modes of this waveguide form a discrete spectrum in the tangential s -direction and a continuous spectrum in the transverse y -direction down the axis of the waveguide,

$$v_n(s, y, t; \kappa) = U_n(s) e^{i\kappa y} e^{-i\omega_n(\kappa)t} , \quad (2.6)$$

$$U_n(s) \equiv \left(\frac{2}{L} \right)^{1/2} \sin(\lambda_n s) , \quad (2.7)$$

for positive mode orders $n = 1, 2, 3, 4, \dots$. The allowed parallel wavenumbers λ_n and the eigenfrequency $\omega_n(\kappa)$ are given by

$$\lambda_n = \frac{n\pi}{L} , \quad (2.8)$$

$$\omega_n^2(\kappa) = (\lambda_n^2 + \kappa^2) V_A^2 . \quad (2.9)$$

The wave is a standing wave in the direction parallel to the magnetic field, with discrete wavenumbers λ_n , and a propagating wave in the y direction with continuous wavenumber κ . The temporal frequency $\omega_n(\kappa)$ depends on both wavenumbers and is illustrated in Figure 2. The parallel eigenfunctions, $U_n(s)$, have been normalized such that they form an orthonormal set.

Our general strategy for solving the driven equation (2.5) is as follows: we will Fourier transform the equation in the invariant y -direction, decompose the source and solution into the eigenfunctions of the waveguide, solve for the amplitude of each mode in spectral space, and then return to configuration space by inverting the transform. After Fourier transforming the driven wave equation and projecting onto the eigenmodes of the waveguide, we obtain

$$\left[\frac{\partial^2}{\partial t^2} + \omega_n^2(\kappa) \right] \hat{v}_n(\kappa, t) = \hat{S}_n(\kappa, t) , \quad (2.10)$$

where

$$\hat{S}_n(\kappa, t) = \int_{-\infty}^{\infty} dy \int_0^L ds S(s, y, t) U_n(s) e^{-i\kappa y} , \quad (2.11)$$

$$\hat{v}_n(\kappa, t) = \int_{-\infty}^{\infty} dy \int_0^L ds v(s, y, t) U_n(s) e^{-i\kappa y} . \quad (2.12)$$

In configuration space, the solution is obtained by inverting the transform and summing over eigenmodes,

$$v(s, y, t) = \frac{1}{2\pi} \int_{-\infty}^{\infty} dy \sum_{n=1}^{\infty} \hat{v}_n(\kappa, t) U_n(s) e^{i\kappa y} . \quad (2.13)$$

A similar equation holds for the reconstruction of the source from its spectral decomposition,

$$S(s, y, t) = \frac{1}{2\pi} \int_{-\infty}^{\infty} dy \sum_{n=1}^{\infty} \hat{S}_n(\kappa, t) U_n(s) e^{i\kappa y} . \quad (2.14)$$

3. Two-Component Signal

We posit that the wave signal seen at the observation location y is a superposition of the waves generated by a source with two components: a broad-band driver that generates a low-amplitude, resonant, background signal and an energetic impulsive source that generates a large initial pulse with subsequent ringing,

$$S(s, y, t) = S_{\text{bg}}(s, y, t) + S_{\text{imp}}(s) \delta(t - t') \delta(y - y') . \quad (3.15)$$

The first term S_{bg} represents the continuous, broad-band driver, which could be the incessant buffeting from ambient waves in the corona external to the waveguide, or perhaps the random movement of the footpoints of the arcade in the photosphere by convective motions. The second term S_{imp} is the impulsive source arising from a single short duration event such as a flare. Of course each source will independently produce a wave response,

$$v(s, y, t) = v_{\text{bg}}(s, y, t) + v_{\text{imp}}(s, y, t) . \quad (3.16)$$

3.1. Resonant Background Oscillations

The background velocity resulting from the broad-band component of the source can be expressed as a superposition of waveguide modes. The amplitude and phase of each mode can be obtained by taking the temporal Fourier transform of equation (2.10), solving for the velocity in spectral space, and inverting the temporal transform through contour integration (see Appendix A),

$$v_{\text{bg}}(s, y, t) = \frac{1}{2\pi} \sum_{n=1}^{\infty} \int_{-\infty}^{\infty} d\kappa A_n(\kappa) U_n(s) \sin[\kappa y - \omega_n(\kappa)t + \theta_n(\kappa)] . \quad (3.17)$$

In this equation, $A_n(\kappa)$ is the mode amplitude of the mode and $\theta_n(\kappa)$ is the phase of the source function in spectral space, evaluated at the mode frequencies,

$$\hat{S}_n^{(\text{bg})}(\kappa, \omega) = \int_{-\infty}^{\infty} dt \int_{-\infty}^{\infty} dy \int_0^L ds S_{\text{bg}}(s, y, t) U_n(s) e^{-i(\kappa y - \omega t)} , \quad (3.18)$$

$$\hat{S}_n^{(\text{bg})}(\kappa, \omega_n) = \left| \hat{S}_n^{(\text{bg})}(\kappa, \omega_n) \right| e^{i\theta_n(\kappa)} , \quad (3.19)$$

$$A_n(\kappa) \equiv \frac{\left| \hat{S}_n^{(\text{bg})}(\kappa, \omega_n) \right|}{\omega_n(\kappa)} . \quad (3.20)$$

The amplitude of the mode $A_n(\kappa)$ depends on the modulus of the source function evaluated at the mode frequency. The factor of frequency appearing in the denominator of the mode amplitude is a direct result of the fact that a white source excites modes such that they all have equal energy. Since the energy in each mode E_n is proportional to both the square of the amplitude $A_n(\kappa)$ and the square of the frequency $\omega_n(\kappa)$, we should expect the amplitude

of each mode to be inversely proportional to its frequency. Even if the source function possesses wavenumber dependence, we still expect the waves with the lowest frequency to dominate the background signal as long as the source is not a rapidly increasing function of wavenumber.

The phase of the response depends on the phase θ_n of the source function and the variation of this phase over all wavenumbers κ comprising the signal. Since the signal has contribution from a range of frequencies around a dominant frequency, we expect the interference between the different frequencies to cause beat patterns that will slowly and randomly rotate the apparent phase of the oscillation in time. Therefore, at a given position along the waveguide, we should expect the resonant background to be dominated by the gravest mode and produce a signal with the following form,

$$v_{\text{bg}} \approx A_{\text{bg}} \sin(\pi s/L) \sin [(\pi V_A/L)t + \phi(t)] , \quad (3.21)$$

where the phase $\phi(t)$ slowly changes with time ($|\dot{\phi}_n| \ll \pi V_A/L$) due to the continual excitation by the source.

We will see that this expectation holds true by exploring in more detail two types of background sources. In Figure 3a we show the source strength (red curve) for a source with a Gaussian dependence on wavenumber,

$$\left| \hat{S}_n^{(\text{bg})}(\kappa, \omega_n) \right| = \tilde{S} \exp \left(-\frac{\kappa^2}{2\Delta^2} \right) \delta_{n1} . \quad (3.22)$$

In this equation, \tilde{S} is an arbitrary constant and Δ is the spectral width of the Gaussian. For simplicity we have assumed that the source only excites the fundamental mode $n = 1$. We model a stochastic source by imposing that the phase of the source $\theta_n(\kappa)$ is a random function with a uniform distribution between 0 and 2π . Figure 3a also shows the mode amplitude $A_n(\kappa)$ as the black curve. This type of source generates an amplitude spectrum that is sharply peaked at zero wavenumber with little contribution from the wings. Thus we expect that the corresponding time-series (shown in Figure 3b) should be dominated by the frequency $\omega_1 = \pi V_A/L$, with a phase that slowly wanders. This is indeed the case. This time-series was constructed by numerically evaluating the inverse spatial transform in Equation (3.17).

For the second source we choose a white source whose strength (by definition) is a constant function of wavenumber. The phase of the source function is once again chosen to be random. Figure 4 presents the amplitude spectrum and the resulting time series. Since

the white source contains a broader range of wavenumbers, it generates a time-series with richer frequency response. In particular, we can clearly see from Figure 4b that the time series possesses high-frequency jitter. The time-series generated by both sources are highly correlated with very similar low-frequency behavior. This is because the same realization of random phases was used to construct both sources. The equivalency of the set of phases also manifests in the temporal power spectra of the two time series (see Figure 5). The fine structure in the two power spectra is similar because this structure arises from wave interference, which of course is determined by the relative phases (which were chosen to be identical).

3.2. Response to an Impulsive Source

The waves generated by the impulsive source are of course determined by the Green's function. Therefore, consider a single point source of unit amplitude that occurs at time t' and at location $(s, y) = (s', y')$. We perform a detailed derivation of the Green's function in Appendix B. The general procedure is to Fourier transform the wave equation in the axial direction y , decompose into waveguide modes, and solve for the temporal behavior. The solution is then reconstructed by summing over mode orders and inverting the spatial Fourier transform. After some manipulation of equation (B9) this inverse transform is expressed as

$$G(s, s', y - y', t - t') = \frac{H(t - t')}{2\pi} \sum_{n=1}^{\infty} \int_{-\infty}^{\infty} d\kappa U_n(s) U_n(s') \frac{\sin[\omega_n(\kappa)(t - t')]}{\omega_n(\kappa)} e^{i\kappa(y - y')} . \quad (3.23)$$

where H is the Heaviside step function. The inverse transform has an analytic solution (Weast et al. 1989) involving zero-order Bessel functions of the first kind, J_0 ,

$$G(s, s'; y - y', t - t') = \frac{H(\tau)}{2V_A} \sum_{n=1}^{\infty} U_n(s) U_n(s') J_0(\lambda_n V_A T) . \quad (3.24)$$

We have written the solution compactly by defining the following delayed times:

$$\tau \equiv (t - t') - \frac{|y - y'|}{V_A} , \quad (3.25)$$

$$T \equiv \sqrt{(t - t')^2 - \frac{(y - y')^2}{V_A^2}} . \quad (3.26)$$

As expected, the Green’s function is nonzero only after the excitation occurs and after the first wave fronts arrive at the observation point (s,y) , i.e., when $\tau > 0$. Further, since both the source and the observation point are within a waveguide, there are many paths that waves can take from the point source at y' to the observation point at y , each reflecting a different number of times from the walls of waveguide (in this case the footpoints). The superposition of waves traveling along all these paths generates the oscillation pattern seen at any given point. This superposition is a combination of waves with different wavenumbers κ and hence directions of initial launch from the source. This summation is represented by the integral in the inverse Fourier transform in equation (3.23).

The response of the waveguide to the impulsive source appearing in equation (3.15), $S_{\text{imp}}(s)\delta(t - t')\delta(y - y')$ is of course the integral of the product of the Green’s function and the source $S_{\text{imp}}(s')$ over the point source’s location s' ,

$$v_{\text{imp}}(s, y, t) = \frac{H(\tau)}{2V_A} \sum_{n=1}^{\infty} \mathcal{A}_n U_n(s) J_0(\lambda_n V_A T) \quad (3.27)$$

$$\mathcal{A}_n \equiv \int_0^L S_{\text{imp}}(s') U_n(s') ds' . \quad (3.28)$$

In Figures 6–8 we show this signal superimposed on the background oscillations. In all cases, the impulsive source occurs at time $t = 0$ and the waves are observed at the apex of the loop $s = L/2$. Further, for simplicity we assume that only the gravest mode $n = 1$ is excited to significant amplitude (i.e., $|\mathcal{A}_n| \ll |\mathcal{A}_1|$ for $n \neq 1$). Figures 6 and 8 correspond to an impulsive event that occurs only a short distance away from the observation point, $\Delta y = y - y' = 0.1 L$, while for Figure 7 the distance between the source and observation point is a one-hundred times larger, $\Delta y = 10 L$. Not only is there increased delay between the event and reception of the first signal for the more distant source, but the fringe pattern is compressed near the time of first arrival. Thus, more distance sources generate signals with a wider range of apparent frequencies.

4. Discussion

We have proposed an alternate model for coronal loop oscillations. Instead of the standard picture that the visible loop is a self-contained 1D oscillator, we propose that the observed waves are MHD fast waves that live on the entire arcade and are inherently 2D in nature. The waves are trapped longitudinally between the loci of field line footpoints in

the photosphere, but freely propagate along the axis of the arcade perpendicular to the field lines. Therefore, the arcade forms a 2D waveguide with modes that have discretized wavenumbers in the longitudinal direction λ_n and continuous wavenumbers κ in the axial direction.

We demonstrate that both the “decaying” flare-induced oscillations and the low-amplitude “decayless” oscillations that have been observed (Nisticò et al. 2013; Anfinogentov et al. 2013) can be explained by such 2D waves if there are two distinct wave sources: a continuous, distributed, stochastic source and a large-amplitude impulsive source, localized both spatially and temporally. For this model, the inclusion of a physical damping mechanism (such as phase mixing or resonant absorption) is not necessary to reproduce the general behavior of either observed wave component. We discuss the properties of the wavefield excited by both of these sources in the following subsections.

4.1. Decayless Oscillations

The decayless oscillations seen by Nisticò et al. (2013) and Anfinogentov et al. (2013) appear to be reproduced with fidelity by considering the effect of a stochastic source that operates throughout the waveguide and continues for long durations. Such a source produces a profusion of waveguide modes with uncorrelated phases. For each longitudinal order n , these modes form a continuous spectrum in the transverse wavenumber κ and therefore frequency ω . Each spectrum has a low frequency cut-off below which no modes exist (see Figure 5). This cut-off corresponds to modes that propagate parallel to the field lines and hence do not travel up and down the waveguide. As such, these modes are those that are most analogous to those that would be obtained in a 1D model where one assumes that thin bundles of field lines are individually resonant.

For a source with wavenumber dependence that is sufficiently flat near $\kappa = 0$, i.e., near the cut-off, we expect that most of the relevant modes saturate such that they have equal energy. Therefore, since the mode energy is proportional to the square of the velocity amplitude and to the square of the frequency, the mode amplitude should be inversely proportional to the mode frequency. This means that the dominant frequency in the spectrum should be the low-frequency cut-off. Thus, in observations we should expect to primarily see the fundamental ($n = 1$) waveguide mode that propagates nearly parallel to the field lines ($\kappa = 0$). This is, of course, exactly what is observed for the large-amplitude flare-induced waves (Aschwanden et al. 1999; Nakariakov et al. 1999), but has yet to be verified for the low-amplitude decayless oscillations.

We further point out that while the spectrum of oscillations is dominated by the mode with the lowest frequency, the wavefield also contains higher frequency components. The relative importance of the high-frequency waves depends on the spectral content of the source. White spectra produce noticeable high-frequency jitter (see Figure 4) whereas a more narrow-band source has a smoother response (see Figure 3). The signal with high-frequency jitter is quite reminiscent of the decayless oscillations presented by Nisticò et al. (2013). Furthermore, the beating and slow modulation of the phase caused by interference between different nearby frequency components is also seen in these observations.

4.2. Flare-Induced Oscillations

A point source located within the waveguide generates a circular wavefront that initially expands isotropically in two-dimensions across the arcade’s magnetic sheet. This isotropic expansion stops, when the wavefront impacts the photosphere and reflection occurs. These reflections then begin to interfere with other portions of the wave front and after many reflections the interference pattern can become rather complicated. Observations made some distance down the waveguide from the point source will see an oscillatory fringe pattern produced by this interference. Thus, the oscillation signal that is seen does not arise from a resonance occurring on the field line where the observation is made. Instead, the oscillation is an interference pattern of many waves as they propagate past the observation point. The initial pulse arises from the segment of the wave front that propagated straight down the waveguide without reflection (i.e., waves with $\kappa \gg \lambda_n$). At later times, the signal is the interference of segments of the initial wave front that have taken different paths down the waveguide, all with the same path length. As time passes the waves that arrive have undergone more and more reflections and therefore have smaller and smaller wavenumber κ . Asymptotically, for very long times all waves contributing to the signal have $\kappa \ll \lambda$ and thus nearly identical frequencies of $\omega_n = \lambda_n V_A$. Thus, the signal stabilizes to the same frequency that one would obtain for a 1D cavity.

One important consequence is that the signal at the observation point decays, but it does not do so because of physical damping. We have not included any dissipation mechanisms in our model. Because of this the decay does not have the exponential fall off with time as one would expect from physical damping. Instead, as indicated by the asymptotic form of the J_0 Bessel function, the signal decreases with time like a power law $1/t^{1/2}$. This decay rate (and the fringe pattern itself) is a direct consequence of the shape of the waveguide and the distance from source to observation point. The shape of the waveguide determines the possible paths and therefore the interference. The distance between source and observation

point is important because the excited waves have differing phase speeds parallel to the axis of the waveguide,

$$\frac{\omega}{\kappa} = \left(1 + \frac{\lambda_n^2}{\kappa^2}\right)^{1/2} V_A . \quad (4.29)$$

Therefore, the waves disperse as they travel down the waveguide and the wave packet elongates and changes shape. Thus, the resulting fringe pattern depends on how far the waves have traveled from the source. This effects manifests as the delayed time $T = \sqrt{\Delta t^2 - \Delta y^2/V_A^2}$ that appears in the argument of the Bessel function.

Finally, we comment that not all observations of flare-driven kink waves have a sudden onset followed by rapid decay. Some appear to grow initially and only afterward begin to decay (see Nisticò et al. 2013; Wang et al. 2012). Such cases are likely the result of a source with a duration that is comparable to or longer than the period of the waves that are excited. The resulting signal would be the temporal convolution of the source with the Green’s function. So, the fringe pattern that would be observed would not only depend on the shape of the waveguide and the distance from the source, but also the duration and temporal variation of the source itself.

4.3. Conclusions

The interpretation of coronal-loop oscillations that we suggest here involves the resonances of a 2D arcade instead of a 1D loop. Therefore, this new picture complicates how mode frequencies might be extracted from an observed time series as the time series has a richer high-frequency spectrum of waves that propagate obliquely to the field. Fortunately, the dominant frequencies correspond to the same type of wave that one would derive from a 1D model. Thus, these frequencies can still be used in a seismic analysis as others have previously envisioned.

While none of our figures have included the signal from higher-frequency overtones ($n > 1$), such modes will certainly be excited. Their exact amplitude depends on the distribution of the driver along the field lines, but in all cases the amplitudes of overtones likely decrease with mode order as high-frequency modes tend to have lower amplitudes even for modes with equal energy. We wish to point out that if one is attempting to measure overtone frequencies from flare-induced oscillations, one must be careful. The response of the fundamental mode of the waveguide to a point source is polychromatic. A wavelet analysis would suggest that the frequency of the oscillation slowly decreases from onset until

an asymptotic value is achieved. A distant source in particular may start oscillating with a rather high frequency compared to its eventual asymptotic value (see Figure 7). It is this asymptotic value that corresponds to the 1D resonant frequencies. Of course in many observations a loop oscillation may only be visible for several cycles and the asymptotic regime may never be reached before the flare-induced signal falls below the background oscillations. Due to the polychromatic nature of flare-induced oscillations, the low-amplitude decayless oscillations may be a better frequency diagnostic as the frequency content of the signal is largely steady with time. This property might allow significant averaging of Fourier (or wavelet) power spectra such that the low-frequency cut-offs that should be present for each mode order become visible and measurable.

Finally, we emphasize that the decay of the flare-induced signal may have nothing to do with physical damping. In our model the decay is a wave interference effect and the resulting fringe pattern is sensitive to the shape of the waveguide. An arcade comprised of loops with a wide variety of lengths should generate a very different fringe pattern and concomitant decay rate than the rectangular waveguide employed here. Further, spatial variation of the Alfvén speed within the waveguide will change the raypaths that combine to form a fringe. Thus with further analysis, the decay rate might prove to be a useful diagnostic of the wavespeed when utilized in tandem with the frequencies.

This work was supported by NASA, RSF (University of Sheffield) and STFC (UK). BWH acknowledges NASA grants NNX08AJ08G, NNX08AQ28G, and NNX09AB04G.

A. Modal Expansion of the Background Signal

In this appendix we provide a derivation of the wavefield generated by a stochastic source that is distributed both spatially and temporally. We do so in a standard way by expressing the solution as a sum over the modes of the waveguide. We begin by considering the contribution to the wavefield that arises from the background source $S_{\text{bg}}(s, y, t)$. The wavefield generated by this source must obey Equation (2.10) with the background source appearing on the right hand side,

$$\left[\frac{\partial^2}{\partial t^2} + \omega_n^2(\kappa) \right] \hat{v}_n^{(\text{bg})}(\kappa, t) = \hat{S}_n^{(\text{bg})}(\kappa, t), \quad (\text{A1})$$

$$\hat{S}_n^{(\text{bg})}(\kappa, t) = \int_{-\infty}^{\infty} dy \int_0^L ds S_{\text{bg}}(s, y, t) U_n(s) e^{-i\kappa y}. \quad (\text{A2})$$

We now take the temporal Fourier transform of these equations, adopting the notation that $f(\omega)$ is the transform of $f(t)$,

$$f(\omega) = \int_{-\infty}^{\infty} dt f(t) e^{i\omega t} . \quad (\text{A3})$$

Note, the opposite sign convention that appears in the oscillatory waveform used in the spatial versus temporal transform. This convention was chosen to ensure that waves with positive wavenumber κ correspond to waves propagating in the positive y direction. After solving for the velocity amplitude, the transform of equation (A1) produces

$$\hat{v}_n^{(\text{bg})}(\kappa, \omega) = -\frac{\hat{S}_n^{(\text{bg})}(\kappa, \omega)}{\omega^2 - \omega_n^2(\kappa)} . \quad (\text{A4})$$

The solution expressed in time t is now obtained by inverting the temporal Fourier transform,

$$\hat{v}_n^{(\text{bg})}(\kappa, t) = -\frac{1}{2\pi} \int_{-\infty}^{\infty} d\omega \frac{\hat{S}_n^{(\text{bg})}(\kappa, \omega)}{\omega^2 - \omega_n^2(\kappa)} e^{-i\omega t} . \quad (\text{A5})$$

This integral can be evaluated by contour integration. Assuming that the source is analytic and lacks poles or continuous spectra, when the contour is deformed downwards in the complex-frequency plane the contribution from the modes is picked up as the residues around the poles of the integrand. There are two poles, one for positive frequencies and the other for negative frequencies, each corresponding to waves propagating in opposite directions up and down the waveguide,

$$\hat{v}_n^{(\text{bg})}(\kappa, t) = \frac{1}{2i\omega_n(\kappa)} \left[\hat{S}_n^{(\text{bg})}(\kappa, \omega_n) e^{-i\omega_n t} - \hat{S}_n^{(\text{bg})}(\kappa, -\omega_n) e^{i\omega_n t} \right] . \quad (\text{A6})$$

For the sake of clarity we have momentarily dropped the explicit κ dependence from the mode frequencies that appear in both the exponentials and the source function.

We now transform back into configuration space by inverting the spatial transform and summing over waveguide modes,

$$v_{\text{bg}}(s, y, t) = \frac{1}{2\pi} \sum_{n=1}^{\infty} \int_{-\infty}^{\infty} d\kappa \left[\frac{\hat{S}_n^{(\text{bg})}(\kappa, \omega_n)}{2i\omega_n(\kappa)} e^{-i\omega_n t} - \frac{\hat{S}_n^{(\text{bg})}(\kappa, -\omega_n)}{2i\omega_n(\kappa)} e^{i\omega_n t} \right] U_n(s) e^{i\kappa y} . \quad (\text{A7})$$

We can put this integral in a more convenient form by making a change of variable in the integral represented by the second term in the square brackets, $\kappa \rightarrow -\kappa'$, and then changing the name of the dummy variable back to the original, $\kappa' = \kappa$. Noting that the eigenfrequencies are symmetric, $\omega_n(-\kappa) = \omega_n(\kappa)$, we obtain

$$v_{\text{bg}}(s, y, t) = \frac{1}{2\pi} \sum_{n=1}^{\infty} \int_{-\infty}^{\infty} d\kappa U_n(s) \left[\frac{\hat{S}_n^{(\text{bg})}(\kappa, \omega_n)}{2i\omega_n(\kappa)} e^{i(\kappa y - \omega_n t)} - \frac{\hat{S}_n^{(\text{bg})}(-\kappa, -\omega_n)}{2i\omega_n(\kappa)} e^{-i(\kappa y - \omega_n t)} \right] \quad (\text{A8})$$

We now use the fact that the source function (in configuration space) is a real function. Therefore, its transform has complex-conjugate symmetry,

$$\hat{S}_n^{(\text{bg})}(-\kappa, -\omega) = \left[\hat{S}_n^{(\text{bg})}(\kappa, \omega) \right]^*, \quad (\text{A9})$$

Using this symmetry property, we can rewrite equation (A8)

$$v_{\text{bg}}(s, y, t) = \frac{1}{2\pi} \sum_{n=1}^{\infty} \int_{-\infty}^{\infty} d\kappa \frac{|\hat{S}_n^{(\text{bg})}(\kappa, \omega_n)|}{\omega_n(\kappa)} U_n(s) \sin[\kappa y - \omega_n(\kappa)t + \theta_n(\kappa)] , \quad (\text{A10})$$

where we have defined the complex phase of the source function evaluated at the mode frequencies,

$$\theta_n(\kappa) \equiv \arg \left\{ \hat{S}_n^{(\text{bg})}(\kappa, \omega_n) \right\} . \quad (\text{A11})$$

B. Calculation of the Green's Function

The Green's function is of course the response of the system to a single point source of unit amplitude. Therefore, consider such a source that occurs at time $t = t'$ and at location $(s, y) = (s', y')$,

$$S(s, y, t) = \delta(s - s') \delta(y - y') \delta(t - t') \quad (\text{B1})$$

The Fourier transform of such a source has the following modal decomposition,

$$\hat{S}_n(\kappa, t) = U_n(s') e^{-i\kappa y'} \delta(t - t') . \quad (\text{B2})$$

If we insert this expression into the right hand side of equation (2.10) we obtain an equation that describes the temporal evolution for each component in the decomposition of the Green's function,

$$\left[\frac{\partial^2}{\partial t^2} + \omega_n^2(\kappa) \right] \hat{G}_n(s', \kappa, \Delta t) = U_n(s') e^{-i\kappa y'} \delta(\Delta t) , \quad (\text{B3})$$

where we have defined $\Delta t \equiv t - t'$. At the time of the excitation event $t = t'$ (or $\Delta t = 0$) the solution must satisfy appropriate jump conditions,

$$\left[\hat{G}_n \right]_{\Delta t=0} = 0 , \quad (\text{B4})$$

$$\left[\frac{\partial \hat{G}_n}{\partial t} \right]_{\Delta t=0} = U_n(s') e^{-i\kappa y'} . \quad (\text{B5})$$

The well-known solution is a sinusoid times a Heaviside step function H ,

$$\hat{G}_n(s', \kappa, \Delta t) = U_n(s') e^{-i\kappa y'} H(\Delta t) \frac{\sin [\omega_n(\kappa) \Delta t]}{\omega_n(\kappa)} . \quad (\text{B6})$$

Because of the particular functional form of $\omega_n(\kappa)$,

$$\omega_n(\kappa) = V_A (\lambda_n^2 + \kappa^2)^{1/2} , \quad (\text{B7})$$

the inverse Fourier transform of the Green's function has a standard solution (Weast et al. 1989) which demonstrates that information travels at a finite speed, i.e., the Alfvén speed V_A ,

$$G_n(s', \Delta y, \Delta t) = \frac{1}{2\pi} \int_{-\infty}^{\infty} d\kappa G_n(s', \kappa, \Delta t) e^{i\kappa y} , \quad (\text{B8})$$

$$= \frac{1}{2\pi} U_n(s') H(\Delta t) \int_{-\infty}^{\infty} d\kappa \frac{\sin [\omega_n(\kappa) \Delta t]}{\omega_n(\kappa)} e^{i\kappa \Delta y} , \quad (\text{B9})$$

$$= \frac{1}{2V_A} U_n(s') H(\Delta t) H(\tau) J_0(\lambda_n V_A T) , \quad (\text{B10})$$

where we have made the following definitions,

$$\tau \equiv \Delta t - \frac{|\Delta y|}{V_A}, \quad (\text{B11})$$

$$T \equiv \sqrt{\Delta t^2 - \Delta y^2/V_A^2}, \quad (\text{B12})$$

$$\Delta y \equiv y - y'. \quad (\text{B13})$$

In this solution, the function J_0 is the zeroth-order Bessel function of the first kind. Since the product of Heaviside step functions in equation (B10) is nonzero only if $\tau > 0$, the Green's function has the following solution in configuration space,

$$G(s, s', \Delta y, \Delta t) = \frac{H(\tau)}{2V_A} \sum_{n=1}^{\infty} U_n(s)U_n(s') J_0(\lambda_n V_A T). \quad (\text{B14})$$

REFERENCES

- Andries, J., Van Doorselaere, T., Roberts, B., Verth, G., Verwichte, E., & Erdélyi, R. 2009, *Space Sci. Rev.*, 149, 3
- Anfinogentov, A., Nisticò, G., & Nakariakov, V.M. 2013, *A&A*, in press
- Aschwanden M. J., Fletcher, L., Schrijver, C. J., & Alexander, D. 1999, *ApJ*, 520, 880
- De Moortel, I. & Brady, C.S. 2007, *ApJ*, 664, 1210
- Goossens, M., Andries, J., & Aschwanden, M.J. 2002, *A&A*, 394, L39
- Goossens, M., Erdélyi, R., & Ruderman, M.S. 2011, *Space Sci. Rev.*, 158, 289
- Nakariakov, V., Ofman, L., DeLuca, E., Roberts, B., Davila, J. M. 1999, *Science*, 285, 862
- Nisticò, G., Nakariakov, V.M., & Verwichte, E. 2013, *A&A*, 552, 57
- Ofman, L. & Aschwanden, M.J. 2002, *ApJ*, 576, 153
- Ruderman, M.S. & Roberts, B. 2002, *ApJ*, 577, 475
- Van Doorselaere, T., Nakariakov, V.M., & Verwichte, E. 2007, *A&A*, 473, 959

Verwichte, E., Nakariakov, V. M., Ofman, L., & Deluca, E. E. 2004, *Sol. Phys.*, 223, 77

Wang, T., Ofman, L., Davila, J.M., & Su, Y. 2012, *ApJ*, 751, L27

White, R.S. & Verwichte, E. 2012, *A&A*, 537, A49

Weast, R.C., et al. 1989, *CRC Handbook of Chemistry and Physics*, 70th edition, ed. R.C
Weast, D.R. Lide, M.J. Astle, W.H. Beyer, (CRC Press: Boca Raton), p. A-84

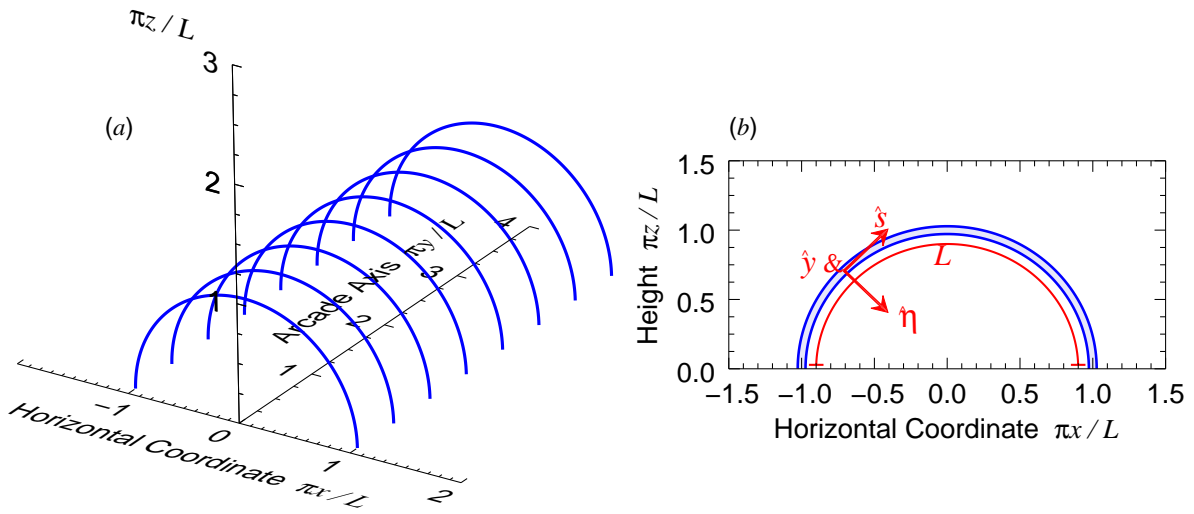


Fig. 1.— Schematic diagram of a coronal arcade. The x - y plane corresponds to the photosphere and the height above the photosphere is given by z . (a) Three-dimensional view of the thin sheet of magnetic field lines that define the arcade. The arcade lacks shear and is invariant along the axis of the arcade in the y -direction. (b) Cross-sectional cut through the arcade at constant y showing a thin annulus. The triad of unit vectors for the local Frenet coordinates are shown in red, with the tangent vector \hat{s} , the principal normal $\hat{\eta}$, and the binormal \hat{y} . Each field line has a length of L from photosphere to photosphere. For the sake of presentation, we assume that each field line forms a semicircle.

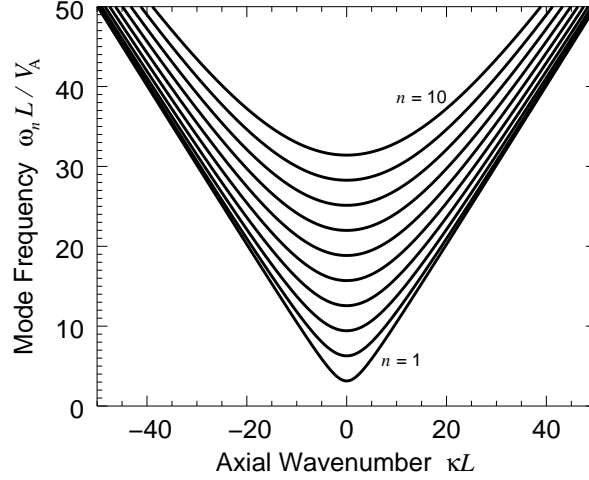


Fig. 2.— The eigenfrequencies, $\omega_n^2 = \lambda_n^2 + \kappa^2$, of the modes of the waveguide as a function of the wavenumber κ parallel to the waveguide’s axis. Each curve corresponds to a different mode order n labelling the discretely allowed wavenumbers $\lambda_n = n\pi/L$ in the direction parallel to the field. The gravest mode ($n = 1$) has the lowest frequency, and each higher order has a correspondingly higher frequency.

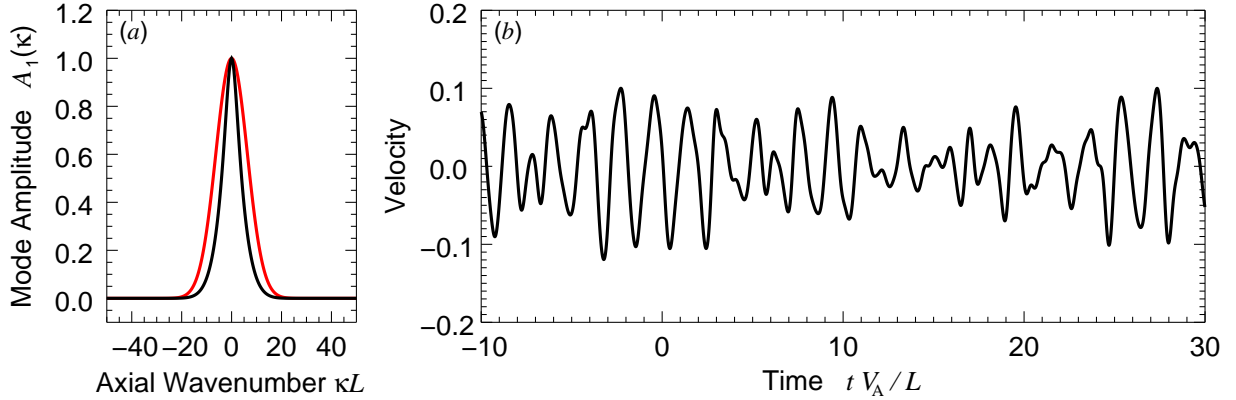


Fig. 3.— The background oscillations described both in spectral space and as a function of time. The source strength $|\hat{S}_1^{(\text{bg})}|$ is a Gaussian function of wavenumber, chosen to have unit amplitude ($\tilde{S} = 1$) and a width of $\Delta = 2\pi/L$. (a) The source strength (red curve) and the resulting amplitude spectrum $A_1(\kappa) = |\hat{S}_1^{(\text{bg})}|/\omega_1(\kappa)$ (black curve) for the gravest mode ($n = 1$) as a function of axial wavenumber κ . (b) The time series of the background oscillation as observed at the apex of the arcade, $s = L/2$, and at an arbitrary position along the arcade $y = y_{\text{obs}}$. The signal has a dominant frequency $\omega = n\pi V_A/L$, with a phase that slowly wanders with time.

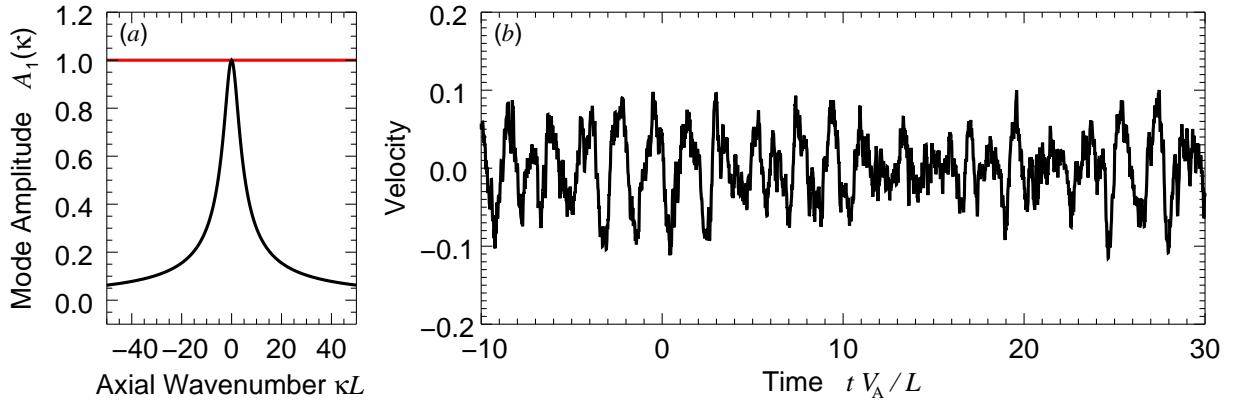


Fig. 4.— The background oscillations described both in spectral space and as a function of time for a source that is white with a strength that is independent of wavenumber. (a) The mode amplitude $A_1(\kappa)$ (black curve) of the background oscillations for the gravest mode ($n = 1$) as a function of axial wavenumber κ . The source strength is overlaid in red. Even though the source is white, the signal is dominated by the waves with the smallest axial wavenumbers and hence the waves with the lowest frequency (see Figure 2). However, the wings of the amplitude distribution are more significant than they are for the Gaussian source. (b) The time series of the background oscillation as observed at the apex of the arcade, $s = L/2$, and at an arbitrary point along the arcade $y = y_{\text{obs}}$. Since the wings are enhanced in the amplitude distribution, the time series has more prominent high-frequency jitter.

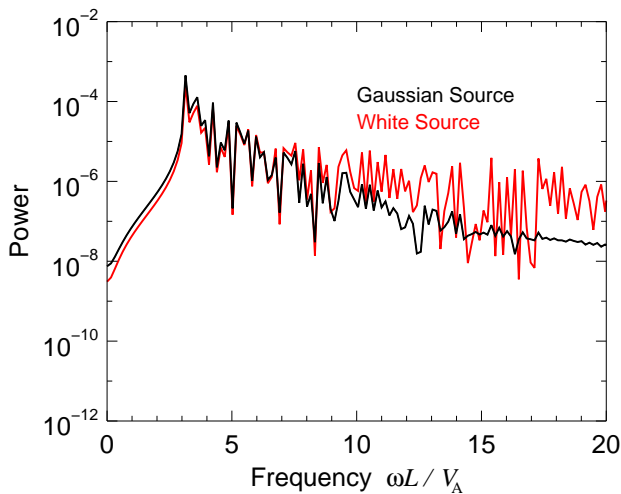


Fig. 5.— Temporal power spectra of the background oscillations illustrated in Figures 3 and 4. The fine structure arises from the interference between waves and is, therefore, sensitive to the specific realization of wave phases. Here, for the sake of comparison, we have used the same realization for both types of source. The spectrum generated by the white source clearly has a greater contribution from high-frequency waves. Both spectra have a low-frequency cut-off that corresponds to the resonant mode frequency $\omega_1 = \pi V_A/L$ appropriate for propagation parallel to the field lines (i.e., $\kappa = 0$).

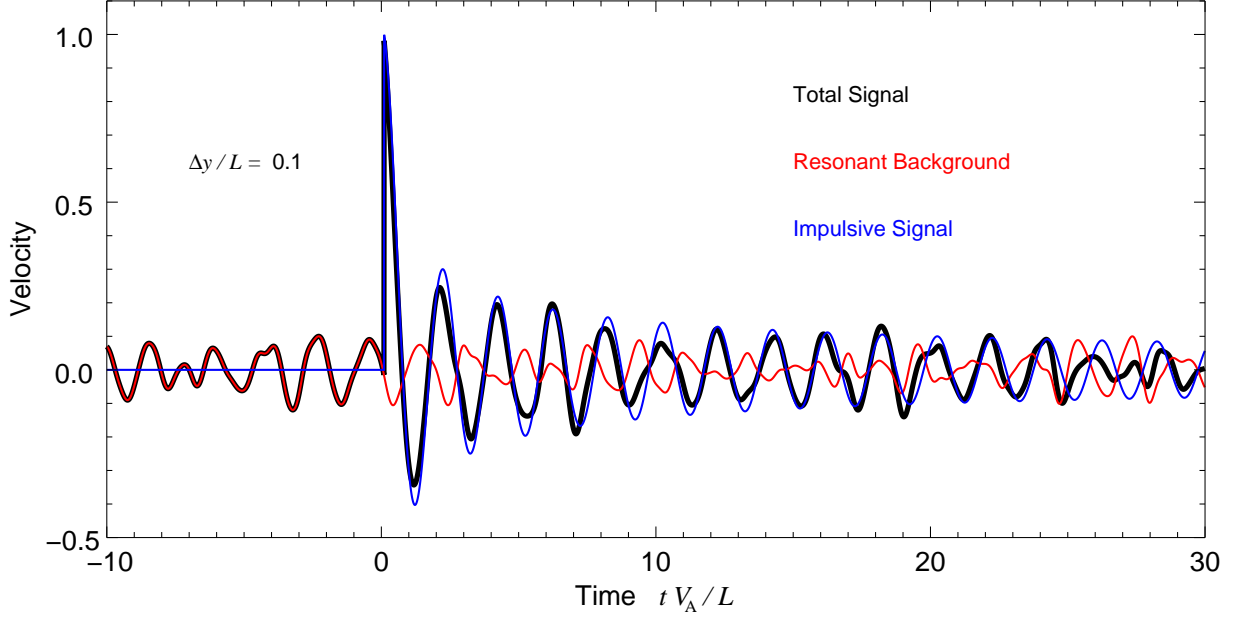


Fig. 6.— The wave signal as a function of time arising from both wave sources. The red curve is the background signal generated by a distributed stochastic source. The strength of the stochastic source is gaussian in wavenumber κ (see Figure 3a). The dominant frequency is the lowest frequency available, corresponding to those waves with $\kappa = 0$ which propagate parallel to the magnetic field. The blue curve is the signal arising from a single impulsive event that occurred rather close to the observation point along the arcade, $\Delta y = 0.1 L$. The initial pulse corresponds to waves that have propagated straight down the waveguide, while the latter oscillations are an interference pattern arising from waves that have taken a variety of paths down the waveguide. The black curve shows the total wave signal. We have chosen the relative size of the impulsive and background sources such that the background has an amplitude of 10% of the initial pulse height of the impulsive signal.

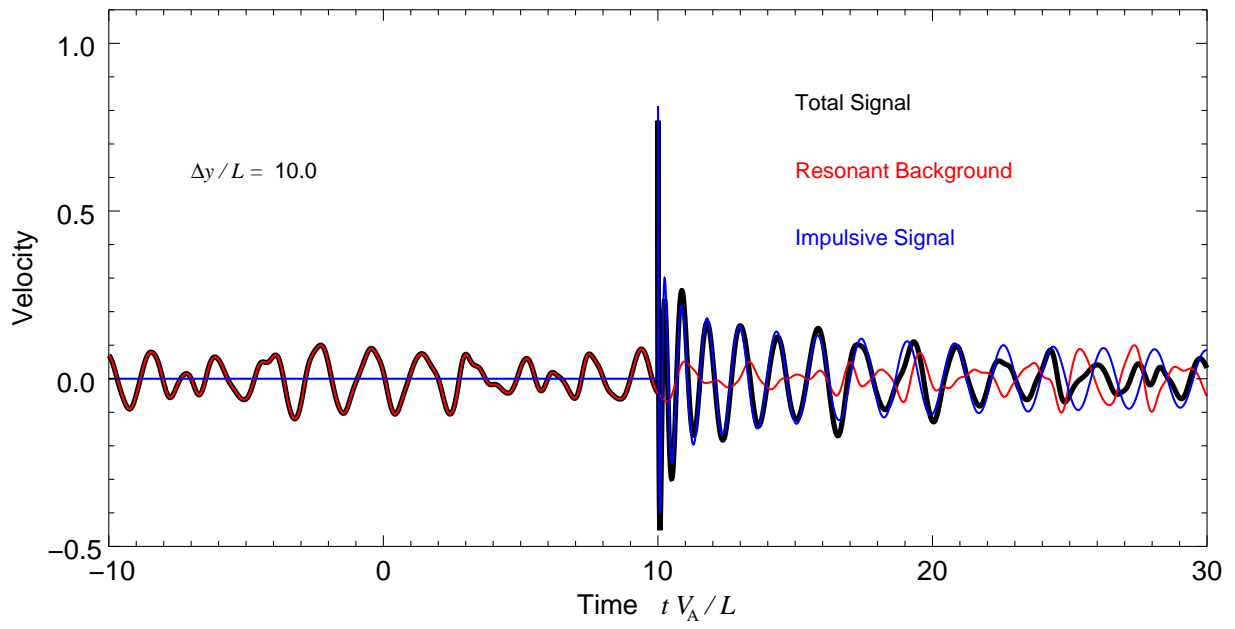


Fig. 7.— As in Figure 6, except the observation point is much farther from the impulsive source, $\Delta y = 10 L$. In addition to the existence of the expected delay required for the waves to arrive at the observation point, the fringes in the interference pattern become compressed in time near the time of first arrival.

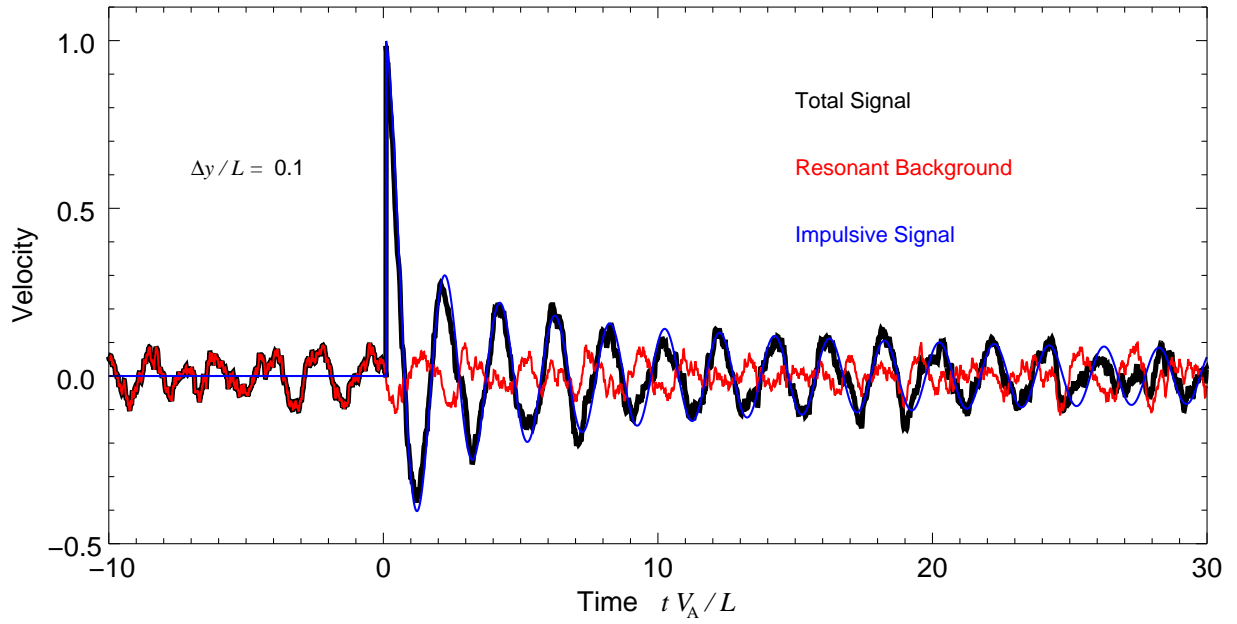


Fig. 8.— As in Figure 6, except the background source is white with equal power in all wavenumbers. The resulting background signal is still dominated by the lowest waveguide frequency, but the relative importance of high frequency waves is clearly visible.